ADVANCED MATERIALS
www.advmat.de

Magnetotransport Anomaly in Room-Temperature Ferrimagnetic $NiCo_2O_4$ Thin Films

*Xuegang Chen, Xiaozhe Zhang, Myung-Geun Han, Le Zhang, Yimei Zhu, Xiaoshan Xu, and Xia Hong**

The inverse spinel ferrimagnetic $NiCo_2O_4$ presents a unique model system for studying the competing effects of crystalline fields, magnetic exchange, and various types of chemical and lattice disorder on the electronic and magnetic states. Here, magnetotransport anomalies in high-quality epitaxial $NiCo_2O_4$ thin films resulting from the complex energy landscape are reported. A strong out-of-plane magnetic anisotropy, linear magnetoresistance, and robust anomalous Hall effect above 300 K are observed in 5–30 unit cell $NiCo_2O_4$ films. The anomalous Hall resistance exhibits a nonmonotonic temperature dependence that peaks around room temperature, and reverses its sign at low temperature in films thinner than 20 unit cells. The scaling relation between the anomalous Hall conductivity and longitudinal conductivity reveals the intricate interplay between the spin-dependent impurity scattering, band intrinsic Berry phase effect, and electron correlation. This study provides important insights into the functional design of $NiCo_2O_4$ for developing spinel-based spintronic applications.

The ferrimagnetic $NiCo_2O_4$ (NCO) possesses high Curie temperature (T_C), high spin polarization, infrared transparency, and high susceptibility to redox reactions,[1–4] making it a promising material candidate for spintronics,[5] optoelectronics,[6] supercapacitors,[7] and electrocatalysis[8,9] applications. NCO has an inverse spinel structure, with the tetrahedral (T_d) cation site occupied by Co and the octahedral (O_h) site equally populated by Ni and Co (**Figure 1**a).[10] The mixed valence of the cations and the coexisting tetrahedral and octahedral oxygen coordinates result in competing electronic and magnetic states, which are further complicated by various types of disorders, including the cation redistribution,[2,10–13] valence state variation,[10,11] oxygen or cation vacancies,[4,5] and antiphase boundaries.[4,14,15] While previous studies of NCO have mainly centered on nanostructured and mesoporous materials,[6–8,15,16] it is of high research interest to examine the system in the epitaxial thin film form, especially for developing spintronic applications such as spinel-based magnetic tunnel junctions (MTJs).[17,18] To date, reports on high-quality NCO thin films have been scarce and mostly focused on the disorder-driven metal–insulator transition,[3,5,11,14,19,20] while the intrinsic magnetotransport properties in the metallic phase remain uncharted.

In this work, we report the magnetotransport anomalies observed in 5–30 unit cell (uc) thick high-quality epitaxial NCO thin films. Below the magnetic ordering temperature, NCO exhibits strong out-of-plane magnetic anisotropy, linear magnetoresistance (MR), and robust anomalous Hall effect (AHE) that persist above room temperature. The longitudinal resistance exhibits a weak temperature dependence that cannot be directly correlated with the magnetic state of the system. The anomalous Hall conductivity (σ_{xy}) shows an unusual nonmonotonic temperature dependence, which changes sign in the thinner films. The relation between σ_{xy} and the longitudinal conductivity (σ_{xx}) at the intermediate temperature range points to the dirty metal behavior in conjunction with the contribution from band intrinsic Berry phase effect, while the low-temperature characteristic can be attributed to disorder-enhanced electron correlation. Our work provides critical information on how to manipulate the competing energy scales in this system to achieve tailored functionalities for spintronic applications.

We deposited high-quality 5–30 uc epitaxial NCO films on (001)-oriented $MgAl_2O_4$ (MAO) substrates. The bulk cubic lattice constant of NCO is 8.128 Å, subjecting to a 0.55% compressive strain when grown on MAO (a = 8.083 Å). X-ray diffraction (XRD) measurements show (001) growth with no impurity phases (Figure 1b). The calculated c-axis lattice constant is 8.196 Å, comparable with the reported values for strained films.[11,19] Figure 1c,d shows the high-angle annular dark-field scanning transmission electron microscopy (HAADF-STEM) images of a 17 uc NCO film, which reveal a homogeneous inverse spinel structure with high crystallinity. Atomic force microscopy (AFM) measurements show smooth surface morphology in these samples (Figure 1e), with typical root mean square roughness of 2–3 Å.

Dr. X. Chen, Dr. X. Zhang, Dr. L. Zhang, Prof. X. Xu, Prof. X. Hong
Department of Physics and Astronomy & Nebraska Center for Materials and Nanoscience
University of Nebraska–Lincoln
Lincoln, NE 68588-0299, USA
E-mail: xia.hong@unl.edu
Dr. M.-G. Han, Dr. Y. Zhu
Condensed Matter Physics and Materials Science Department
Brookhaven National Laboratory
Upton, NY 11973-5000, USA
The ORCID identification number(s) for the author(s) of this article can be found under https://doi.org/10.1002/adma.201805260.

DOI: 10.1002/adma.201805260

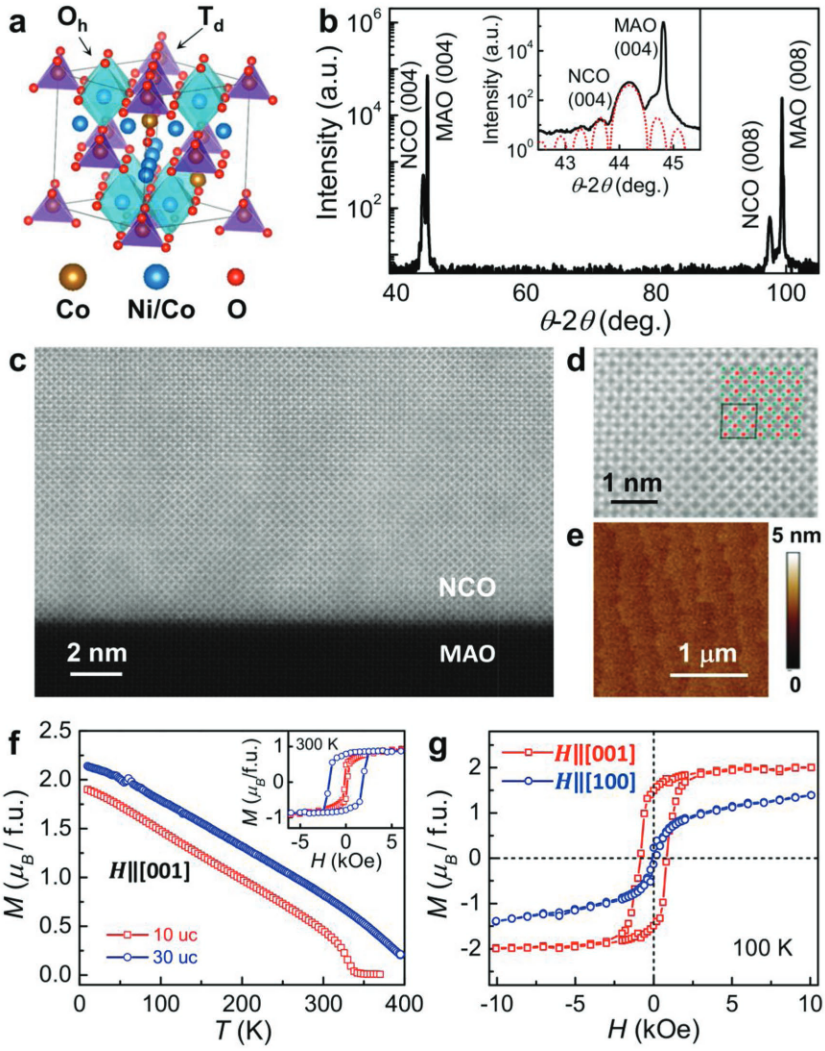

Figure 1. Characterizations of NCO films. a) Schematic crystal structure of NCO. b) XRD θ–2θ scan of a 30 uc NCO. Inset: expanded view around the (004) peak with fits to the Laue oscillations. c) HAADF-STEM image taken on a 17 uc film, and d) a higher-magnification image labeled with the atomic arrangements at the T_d (red dots) and O_h (green dots) sites. e) AFM topography image of a 25 uc NCO film on MAO. f) Out-of-plane M vs T for 10 and 30 uc films. Inset: M vs H at 300 K. g) M vs H in out-of-plane and in-plane magnetic fields for the 10 uc film at 100 K.

Figure 1f shows the out-of-plane magnetization (M) as a function of temperature for two NCO films after saturating the magnetization at low temperature. The magnetic transition temperature for the 10 uc (≈8.2 nm) film is about 340 K. Below T_C, M increases monotonically with decreasing temperature, and reaches ≈1.9 μ_B per formula unit (f.u.) at 10 K. For the 30 uc (≈24.6 nm) film, T_C is above 395 K, which is the highest value reported on epitaxial NCO films,[11,14,19,20] attesting the high quality of our samples. Both the 10 and 30 uc films exhibit robust M–H hystereses at 300 K (Figure 1f, inset), with the coercive field H_c of about 150 Oe and 1.85 kOe, respectively. Figure 1g shows the M–H hystereses for the 10 uc sample at 100 K. In the out-of-plane magnetic field, magnetization saturates at ≈2 μ_B per f.u., in good agreement with the optimal value. The 30 uc sample, on the other hand, exhibits an enhanced saturation moment of ≈2.2 μ_B per f.u. at low temperature. In NCO, the valence distribution can be written as $Co_x^{2+}Co_{1-x}^{3+}[Co^{3+}Ni_{1-x}^{2+}Ni_x^{3+}]O_4^{2-}$, where the magnetic moments of the T_d-site Co and the O_h-site Ni ions are antiferromagnetically coupled. The optimal net moment is 2 μ_B per f.u., given by either the combination of T_d-site Co^{3+} (4 μ_B per f.u.)/O_h-site Ni^{2+} (2 μ_B per f.u.) or T_d-site Co^{2+} (3 μ_B per f.u.)/O_h-site Ni^{3+} (1 μ_B per f.u.), thus independent of the valence state distribution x.[11] The intermixing of equivalent T_d-site Co and O_h-site Ni cations also does not affect the saturation moment, while oxygen vacancies only reduce the moment value. An enhanced magnetic moment can only originate from a suppressed O_h-site moment, either through a higher Co concentration, as Co^{3+} at the O_h site is in the diamagnetic low-spin state ($S = 0$), or through the formation of Ni vacancies. The former mechanism is energetically more favorable as it does not perturb the crystal structure. This assessment is consistent with the fact that no appreciable presence of cation vacancies has been observed in the STEM images (Figure 1c,d).

In an in-plane magnetic field, the magnetization for the 10 uc film does not saturate in up to 10 kOe magnetic field (Figure 1g), confirming that the magnetic easy axis is out of plane. The strong perpendicular magnetic anisotropy is observed in films of all thicknesses, which can be attributed to the effect of compressive strain imposed by the MAO substrate (Figure S1, Supporting Information), and is highly desirable for developing low-power, high-speed magnetic memory.[21] This property, along with the high T_C, high spin polarization, and good lattice match with MAO, a promising material candidate for high-performance tunnel barriers,[18] makes NCO an ideal choice as the spin injection layer for spinel-based epitaxial MTJs.[17]

We next examined the magnetotransport properties of the NCO films. **Figure 2**a shows the temperature dependence of the longitudinal sheet resistance $R_\square$ measured with current along the [110] direction (Figure S2, Supporting Information) for NCO films with different thicknesses. All samples exhibit metallic conduction ($dR/dT > 0$) upon cooling followed by a moderate resistance upturn at low temperature, which cannot be described by a simple localization model. For the 10–30 uc films, the temperature of minimum resistance T_{min} is about 37–40 K, lower than those reported in the literature.[11,19,20] This resistance upturn has previously been attributed to the disorder-enhanced electron correlation effect in a 3D system.[20] The weak thickness dependence of T_{min} also confirms that this transition is not due to the finite size effects such as the electric dead layer[22] or reduced dimensionality.[23] The 5 uc film,

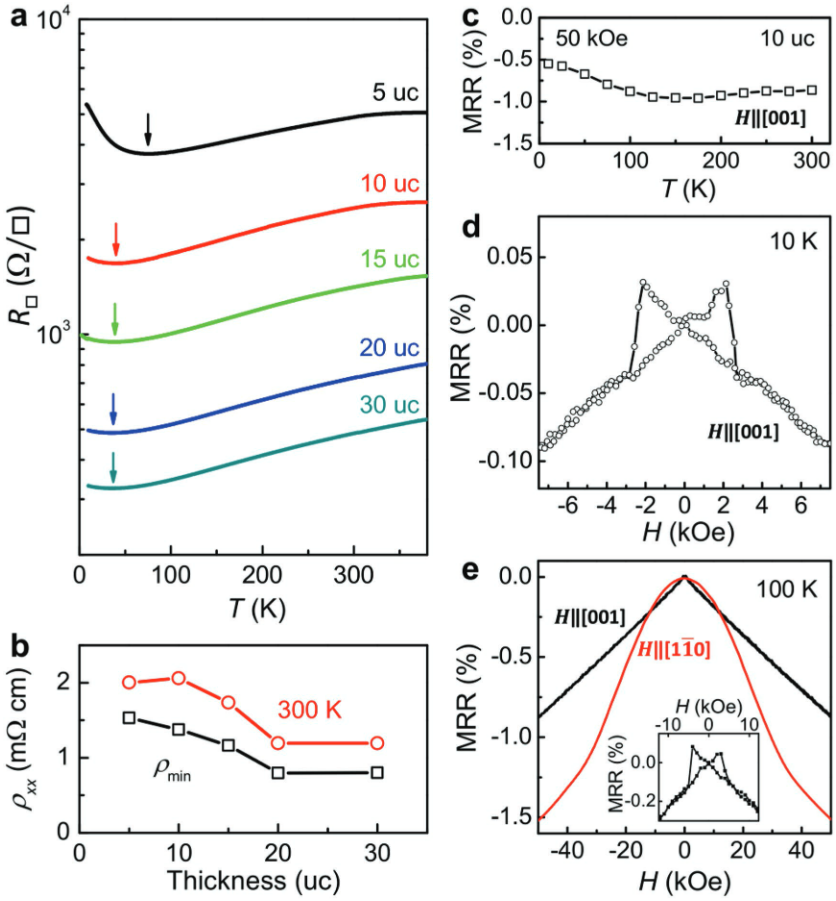

Figure 2. Magnetoresistance of NCO films. a) $R_\square(T)$ for films with different thicknesses. The arrows mark T_{min}. b) ρ_{xx} at 300 K and the minimum ρ_{xx} value vs film thickness. c–e) MRR for a 10 uc film: c) MRR at $H_\perp$= 50 kOe vs T, d) MRR vs $H_\perp$ at 10 K, and e) MRR vs H at 100 K in out-of-plane and in-plane magnetic fields, with both perpendicular to the current direction [110]. Inset: out-of-plane MRR hysteresis at low field.

on the other hand, exhibits considerably higher T_{min} (≈70 K) and enhanced resistivity ρ_{xx} (Figure 2a,b). Such suppressed metallicity, along with the lower magnetic ordering temperature, in the ultrathin limit has been widely observed in epitaxial correlated oxide thin films, while the driving mechanism can be associated with the thickness-driven dimensionality crossover,[23] energy gap formation due to enhanced correlation,[24] and/or variation in the oxygen octahedral distortion at the surface/interface.[25,26] In all films, the longitudinal resistivity exhibits very weak T-dependence, with the residue resistance ratio $\rho_{xx}(T_{min})/\rho_{xx}(300\ K)$ ranging from 0.67 to 0.77, which is the signature behavior of a multiband conductor with both electron and hole bands close to the Fermi level (E_F).[4] Unlike previous reports,[11,19,20] our samples do not exhibit a metal–insulator transition at high temperature, retaining the metallic conduction even above T_C. The lowest resistivity value is ρ_{min} = 0.8 mΩ cm (Figure 2b), which is among the best results reported for epitaxial NCO films.[11,14,19,20]

Overall, the NCO films exhibit a very small negative MR. Figure 2c–e shows the MR ratio, defined as MRR = $[R_{xx}(H) - R_{xx}(0)]/R_{xx}(0)$, taken on the 10 uc sample. In an out-of-plane magnetic field of 50 kOe, MRR is <1% over the entire temperature range (Figure 2c), significantly lower than previously reported values.[5,14,15,19] This small MR rules out a strong presence of phase separation[5] or antiphase boundaries,[14,15] further attesting the structural and phase homogeneity of the NCO films. At low fields, the MR exhibits sharp resistance switching hysteresis due to the magnetization reversal (Figure 2d,e). For both out-of-plane and in-plane magnetic fields, MR shows no sign of saturation in magnetic fields up to 50 kOe (Figure 2e), well above the coercive field. The MR is anisotropic, with the in-plane and out-of-plane MR exhibiting distinct field dependences. The in-plane MR evolves from quadratic to convex dependence with increasing magnetic field, which is typical in magnetic oxides along the magnetic hard axis[27] and can be attributed to the suppressed spin scattering in magnetic field. The out-of-plane MR, in sharp contrast with those observed in structurally or magnetically inhomogeneous samples,[5,14,15] exhibits an apparent linear H-dependence. This unconventional linear MR, like the anomalous Hall effect, originates from the momentum space Berry curvature. Previous studies of disordered magnetic conductors ($\omega_c\tau << 1$) via semiclassical Boltzmann theory have shown that the Berry curvature and associated orbital moment can lead to an intrinsic linear MR, with the sign depending on the position of E_F in the energy bands.[28] This effect is only observed in the out-of-plane MR when spin fluctuation is quenched due to the strong perpendicular anisotropy.

Below T_C, the Hall resistance R_{xy} of NCO shows robust switching hysteresis in the out-of-plane magnetic field $H_\perp$, signaling the anomalous Hall effect. **Figure 3**a shows the Hall resistivity ρ_{xy} as a function of $H_\perp$ at 300 K, where the hystereses are clockwise for films of all thicknesses. The Hall signal can be decomposed into two terms[29]

$$\rho_{xy} = R_0 H_\perp + \rho_A \quad (1)$$

with $\rho_A = 4\pi R_S M_\perp$. Here R_0 and R_S are the normal and anomalous Hall coefficients, respectively, and $M_\perp$ is the out-of-plane magnetization. The anomalous Hall resistivity ρ_A, following the convention of normal Hall effect, is defined as positive for a counterclockwise hysteresis. At 300 K, ρ_A is negative, with the magnitude increasing with the film thickness, varying from 1.2 μΩ cm for the 5 uc film to 2.1 μΩ cm for the 30 uc film (Figure 3b). The corresponding coercive field increases from 75 Oe to 2.2 kOe (Figure 3c), corroborating the higher T_C in thicker films. The robust AHE at room temperature, along with the high sensitivity of H_c to the film thickness, points to an effective route for designing the switching time and power of NCO-based MTJs.

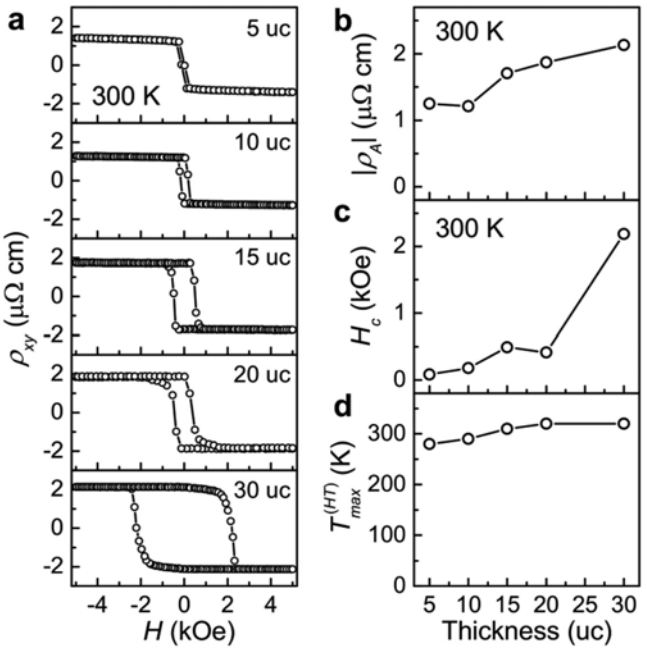

Figure 3. Room-temperature AHE. a–c) ρ_{xy} vs $H_\perp$ hystereses at 300 K for NCO films with different thicknesses (a), with corresponding $|\rho_A|$ (b) and H_c (c) as functions of film thickness. d) Temperatures at which the high-temperature maximum $|\rho_A|$ occurs vs film thickness.

Despite the evolving magnetic energy, NCO films of all thicknesses exhibit a nonmonotonic T-dependence in the AHE signal, with the high temperature $|\rho_A|$ peaking around room temperature (Figure 3d and Figure S3 in the Supporting Information). **Figure 4**a shows the hystereses of the Hall resistance $R_{xy}(H)$ taken on a 30 uc film at different temperatures. Below T_C, the magnitude of ρ_A first increases with decreasing temperature, reaching the maximum value at 320 K. This initial rise can be correlated to the sharp increase of the magnetization right below T_C. As $M(T)$ evolves into a slower growth, $|\rho_A|$ starts to decrease upon cooling (Figure 1f). Similar high-temperature behavior is also observed in the 10 uc sample (Figure 4b). What is interesting is the distinct low-temperature $\rho_A(T)$ observed in these two films (Figure 4c). Below 100 K, the T-dependence of ρ_A in the 30 uc film becomes gradually weaker, which eventually saturates at about –0.4 μΩ cm, retaining the negative sign (clockwise hysteresis of ρ_{xy}) over the entire temperature range. In sharp contrast, for the 10 uc sample, the clockwise AHE hysteresis diminishes entirely at ≈190 K. When the hysteresis re-emerges at lower temperature, it is in the counterclockwise direction, corresponding to a positive ρ_A with increasing magnitude. Despite the sign change, the transition of ρ_A at 190 K for the 10 uc sample is smooth with no abrupt changes in the magnitude, nor are there any kinks in ρ_{xx} (Figure 2a) or M (Figure 1f). The sign change in ρ_A has been observed in all thinner samples (5–20 uc). Measurements of three 10 uc samples yield identical $\rho_A(T)$, confirming that the effect is robust (Figures S2 and S4, Supporting Information).

In recent years, AHE has been widely exploited as a powerful tool to probe the emergent magnetism and/or topological phases in nanoscale magnetic materials,[30–38] while such sign change in ρ_A driven by both thickness and temperature has not been observed in any single-phase material. Identifying the underlying mechanism is critical for the technological implementation of the AHE for spintronic applications. We first note that there is a strong correlation between the T-dependences of the AHE signal and the coercive field. Figure 4d shows the H_c data extracted from the hystereses of AHE and magnetization (Figure S5, Supporting Information), with both methods yielding similar results. For the 10 and 30 uc films, H_c exhibits a rapid increase below

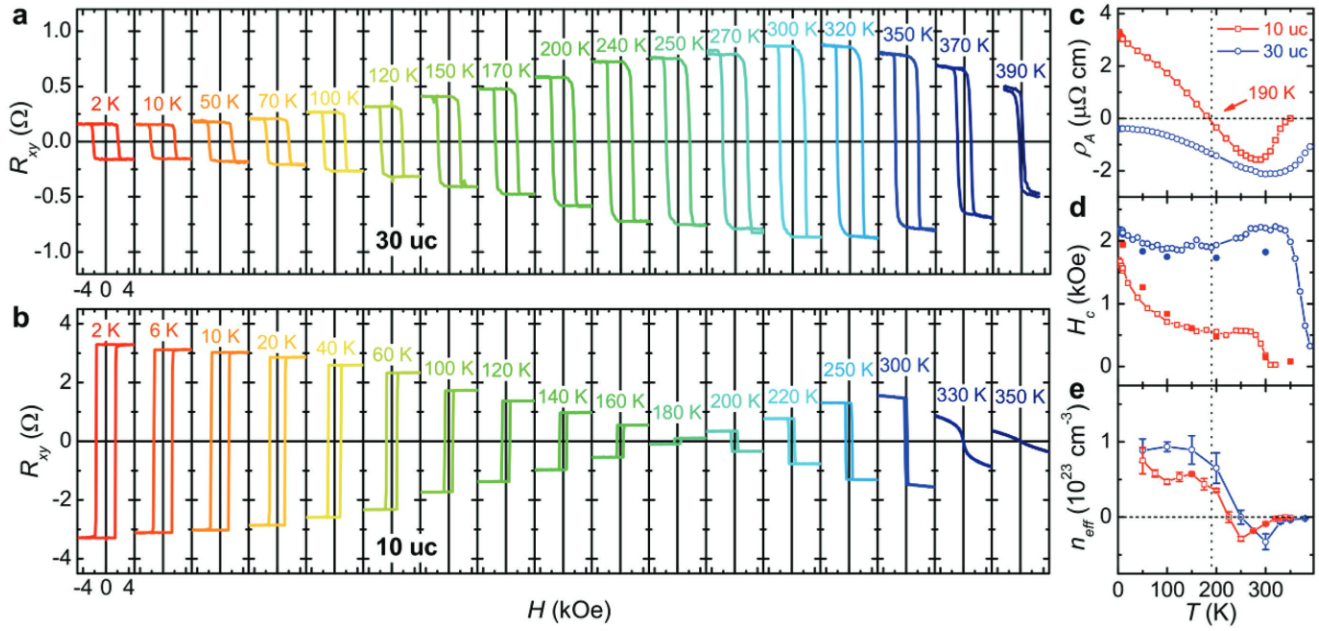

Figure 4. a,b) Temperature dependence of the Hall effect. R_{xy} vs $H_\perp$ hystereses at different temperatures for a 30 uc NCO film (a) and a 10 uc NCO film (b). c–e) ρ_A values (c), H_c extracted from the AHE (open symbols) and $M(H)$ data (solid symbols) (d), and n_{eff} (e) as functions of temperature for the 10 and 30 uc films.

T_C, concomitant with the initial rise in $|\rho_A|$ (Figure 4c). Once $|\rho_A|$ reaches the maximum value, H_c for the 30 uc film settles at about 2 kOe, consistent with previously reported values for optimal samples.[5,20] The 10 uc film, in sharp contrast, exhibits an exponential growth in H_c, corresponding to thermally activated domain wall (DW) depinning.[39] Below 10 K, both samples exhibit similar H_c of ≈2 kOe, indicating comparable magnetic anisotropy energy. The distinct $H_c(T)$ thus points to a strong presence of disorder potential in the thinner film that contributes to DW pinning. As AHE depends sensitively on the interplay between the band intrinsic Berry curvature and spin-dependent impurity scattering,[29] the thickness dependence of AHE may also result from the evolving strength of the disorder energy in the system.

The varying disorder effect, however, cannot account for the unusual T-dependence of AHE. As NCO is a multiband conductor,[4] a possible scenario for the sign change in ρ_A is thermal effect–induced band crossing, which changes the effective carrier type in the system. Figure 4e shows the T-dependence of the effective carrier density in the 10 and 30 uc samples extracted from the normal Hall coefficient R_0 at high field (up to 50 kOe), $n_{eff} = 1/eR_0$. For both samples, R_0 evolves from electron-like (negative) at high temperature to hole-like (positive) at low temperature. This temperature-driven carrier type change was observed in samples of all thicknesses. The transition temperature $T_{SC}^{(n)}$ ranges from 200 to 250 K with no apparent dependence on the film thickness (**Figure 5**a), consistent with a band-crossing picture due to the thermal effect on the lattice. Except the 30 uc sample, where ρ_A does not change sign over the entire temperature range, the carrier type crossover for all thinner films occurs well above the sign change temperature for AHE $T_{SC}^{(AH)}$, with the latter exhibiting an apparent thickness dependence. We thus rule out the direct correlation between the sign changes in the normal and anomalous Hall effects.

Other possible scenarios that can flip the sign of ρ_A include the competition between bulk, surface, and interface contributions[40,41] and the reversal of the Berry curvature as E_F goes through the band-crossing point due to spin–orbit interaction.[30] The former scenario can account for the AHE in Co/Pd multilayers, where the T-dependent mean free path is comparable with the film thickness.[40,41] The latter has been employed to explain the temperature/doping-driven sign change in the ruthenates[30,42–44] and ferromagnetic semiconductors.[38,45,46] These effects, however, are expected to occur in superclean samples, and the second scenario predicts a scaling relation between σ_{xy} and the magnetization,[30,43] which does not apply to our samples (Figure S6, Supporting Information).

Considering the smooth T-dependences of the magnetization (Figure 1f), ρ_{xx} (Figure 2a), and ρ_A (Figure 4c) around $T_{SC}^{(AH)}$, we propose that there are at least two mechanisms contributing to the AHE signal in NCO, with opposite signs and distinct T-dependences, whose competition leads to the sign change in the net AHE. Due to the complexity of the multiband system, simple analysis of the relation between R_S and ρ_{xx} as extended from Equation (1) is not applicable to NCO. The AHE in multiband magnetic conductors has previously been modeled by quantum transport theory,[46–50] which predicts the characteristic scaling behaviors of the anomalous Hall conductivity σ_{xy} depending on the relative strength of the scattering rate h/τ with respect to the Fermi energy E_F. In the moderately dirty region ($h/\tau \leq E_F$), the AHE signal is dominated by the band intrinsic Berry phase contribution, with $\sigma_{xy} \approx \rho_{xy}/\rho_{xx}^2$ insensitive to impurity scattering and independent of the longitudinal conductivity σ_{xx}.[47] In the dirty regime ($h/\tau \geq E_F$), σ_{xy} exhibits a universal, power-law dependence on σ_{xx} : $\sigma_{xy} \propto \sigma_{xx}^{1.6}$.[47,50] Close to this boundary, these two mechanisms can lead to AHE signals with comparable magnitudes.[49] In this model, the conductivity of the NCO films ($\sigma_{xx} \sim 10^3$ S cm^{-1}) lies close to the boundary between the dirty and moderately dirty regions. We thus propose a universal scaling relation that takes both contributions into account

$$\sigma_{xy} = A\sigma_{xx}^{1.6} + \sigma_{xy}^{(0)} \quad (2)$$

where the first and second terms depict the dirty regime scaling behavior[50] and the scattering-independent band intrinsic contribution,[47–49] respectively, and A is a fitting parameter. In Figure 5d, we plot σ_{xy} vs σ_{xx} for films of all thicknesses and superimpose on the data the fits to Equation (2). The data within the initial high-temperature rise in $|\rho_A|$ (Figure 4c) are not included to avoid the effect of enhanced spin fluctuation close to T_C. In the intermediate temperature

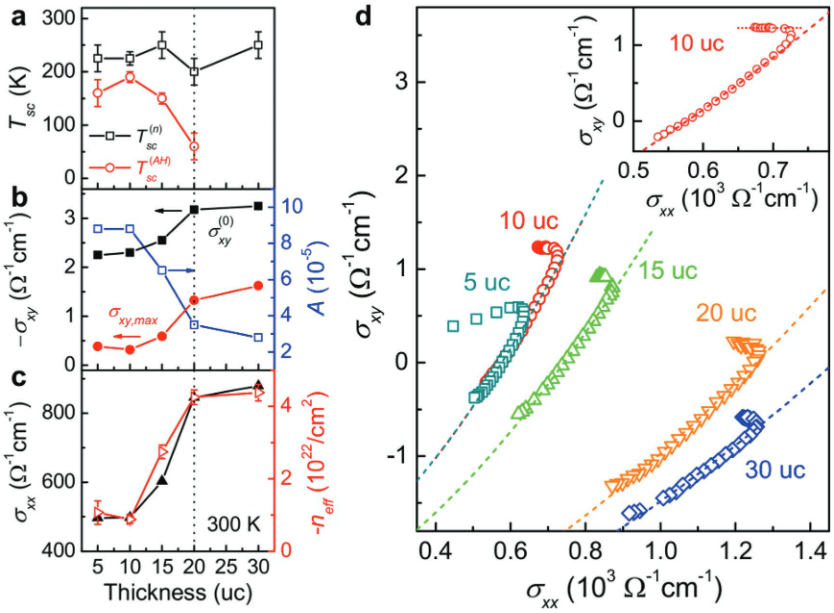

Figure 5. Effect of film thickness on AHE. a) Film thickness dependence of sign change temperatures for ρ_A and R_0. b) Film thickness dependence of (left axis) $-\sigma_{xy}^{(0)}$ (black solid squares), maximum σ_{xy} value at high temperature (red solid circles), and (right axis) the fitting parameter A to Equation (2) (blue open squares). c) Film thickness dependence of (left axis) σ_{xx} (black solid symbols) and (right axis) effective electron density (red open symbols) at 300 K. d) σ_{xy} vs σ_{xx} for NCO films of difference thicknesses with fits to Equation (2) (dashed lines). Inset: σ_{xy} vs σ_{xx} for the 10 uc film with fit (dashed line). The dotted line serves as a guide to the eye.

regime, the AHE signal for all samples can be well described by Equation (2), which captures the smooth change in σ_{xy} at $T_{SC}^{(AH)}$. In this scenario, the sign change in the net σ_{xy} simply results from the growing strength of the first term with decreasing temperature, where the sample conductivity is enhanced due to suppressed phonon scattering. The extracted intrinsic contribution is $\sigma_{xx}^{(0)} \approx 2$–$3\ \Omega^{-1}\ \mathrm{cm}^{-1}$ (Figure 5b), comparable with those observed in ferromagnetic semiconductors but occurring at much higher temperatures.[46]

This scenario, in conjunction with the enhanced disorder in thinner films, also naturally accounts for the thickness dependence of the AHE. As shown in Figure 5b, the 30 and 20 uc samples possess similar values of the intrinsic $\sigma_{xx}^{(0)}$, which is gradually suppressed in thinner samples. The abrupt drop in the band intrinsic contribution is accompanied by the substantially reduced σ_{xx} and n_{eff} in films thinner than 20 uc (Figure 5c), which can be attributed to a modified band structure due to the finite size effect.[22–24] Since the high-temperature, negative anomalous Hall signal depends sensitively on the intrinsic contribution (Figure 5b), identifying this thickness boundary for the finite size effect is critical for designing the AHE for room-temperature applications. Below $T_{SC}^{(AH)}$, the AHE is dominated by the impurity scattering term. In line with the suppressed $\sigma_{xx}^{(0)}$ in the thinner films is an enhanced coefficient A (Figure 5b), which signals the growing strength of impurity scattering.

We next consider the AHE-relevant scattering sources in NCO that are enhanced in thinner films. NCO is intrinsically disordered due to the valence distribution of the cations and intermixing of the Ni and Co at the O_h sites.[2,10–13] At finite temperature, the thermally excited spin fluctuation can also contribute to scattering, as the quasilinear T-dependence of magnetization suggests that spin fluctuation is not fully quenched even down to 10 K (Figure 1f). However, neither mechanism shows any apparent dependence on the film thickness. The small MR and optimal magnetization in the thinner films further rule out a stronger presence of structural and phase inhomogeneity.[5,14,15] Also, we do not expect a variation of the strain state in this thickness range, as previous studies have shown that films on MAO substrates remain fully strained with up to 700 nm thickness.[20] More insights can be gained by correlating the AHE result with the $H_c(T)$ data (Figure 4c,d). The 30 uc sample exhibits nearly T-independent H_c below 300 K, indicating that the relative strength of the anisotropy energy well exceeds the thermal energy. This is consistent with the fact that the band intrinsic contribution dominates in the entire temperature regime. As to the 10 uc sample, in the temperature regime where the impurity scattering term dominates ρ_A, $H_c(T)$ concomitantly exhibits a thermally activated DW depinning behavior,[39] suggesting that the type of disorder that causes DW pinning can also be relevant to spin scattering. The enhanced contribution from the surface/interface state presents a natural source for DW pinning in thin films,[20] which can also affect spin scattering.[40,41]

One consequence of the coexisting contributions to the AHE is that there is a high-temperature local maximum in $|\sigma_{xy}(T)|$ occurring right around room temperature (Figure 4a–c), which is an ideal scenario for designing spintronic devices. For thinner films that exhibit the sign change in AHE, there is a second maximum at low temperature close to the resistance minimum. For the 10 uc film, $|\sigma_{xy}|$ reaches the low-temperature maximum value of about $1.2\ \Omega^{-1}\ \mathrm{cm}^{-1}$ at ≈40 K. As the temperature is further lowered, the σ_{xy} vs σ_{xx} relation changes drastically. As shown in Figure 5d, below $T_{\min}$, the power-law dependence diminishes and σ_{xy} evolves to be a constant $\sigma_{xy}^{(1)}$ for all samples thicker than 5 uc. As the sample conduction in this regime is dominated by disorder-enhanced electron–electron interaction,[20] another possible scenario for dissipation-independent σ_{xy} is the side jump effect.[47,50–52] Assuming the band intrinsic term is still present, the side jump contribution $\sigma_{xy}^{(sj)} = \sigma_{xy}^{(1)} + \sigma_{xy}^{(0)}$ is positive (Figure S7, Supporting Information), which is also opposite to the band intrinsic term. However, given the limited σ_{xx} variation in this regime, we cannot rule out the possibility that the weak σ_{xx}-dependence is a transition behavior, or the enhanced electron correlation modifies the Berry curvature of the band. For the 5 uc film, on the other hand, σ_{xy} slightly decreases with temperature, which may be due to phonon-assisted hopping[53] or enhanced disorder correlation as the film approaches the electric dead layer thickness.[52] For both types of behaviors, future experiments at temperatures below 2 K and additional theoretical insights on the effect of electron correlation are required to fully understand the AHE at the low-temperature regime.

In conclusion, we report robust AHE in high-quality epitaxial NCO thin films as thin as 5 uc (≈4 nm), with the anomalous Hall resistance peaking around room temperature. The unusual temperature and film thickness dependences of the AHE reveal the complex interplay of the band intrinsic Berry curvature, electron correlation, and various disorders. We also identify the critical size effect in determining the magnetic ordering temperature, coercive field, and the magnitude and sign of the AHE response, providing an effective material strategy for engineering the data coding, switching dynamics, and power consumption in NCO-based spintronic applications.

Experimental Section

Sample Growth and Characterization: Epitaxial NCO films were deposited on MAO substrates (5 mm × 5 mm × 0.5 mm) via off-axis radio frequency magnetron sputtering at 320 °C in 100 mTorr process gas ($Ar:O_2$ = 1:1). The XRD measurements were performed on a Rigaku SmartLab diffractometer. The sample surface morphology was characterized using a Bruker Multimode 8 atomic force microscope. The magnetization measurements were performed via SQUID magnetometry (Quantum Design Magnetic Property Measurement System). The diamagnetic background signal was subtracted based on the high-temperature data (Figure S5, Supporting Information).

HAADF-STEM Measurements: A cross-section TEM sample of the thin film heterostructure was prepared for STEM using focused-ion beam (FIB) technique. The final milling was performed with 2 keV Ga^+ to reduce ion-beam-induced damage. A JEOL ARM 200CF with a cold field emission gun and double-spherical aberration correctors at the Brookhaven National Laboratory was used for HAADF-STEM with 200 keV imaging electrons. The range of detection angle for HAADF-STEM was from 68 to 280 mrad.

Device Fabrication and Characterization: Both Hall bar fabricated via optical lithography and van der Pauw geometries were employed to measure the Hall effect, with the current applied along the [110] orientation. The Hall bar devices have channel length of 600 µm and width of 200 µm. Both geometries give consistent results (Figure S2,

Supporting Information). The magnetotransport studies were carried out using a Quantum Design Physical Property Measurement System combined with external Keithley 2400 SourceMeter and standard lock-in technique (SR830) at the temperature range of 2–390 K and magnetic fields up to 5 T. Low excitation current (≤10 μA) was used to avoid Joule heating.

Supporting Information

Supporting Information is available from the Wiley Online Library or from the author.

Acknowledgements

The authors would like to thank Alexey Kovalev, Allan MacDonald, and Qian Niu for valuable discussions and Ethan Gubbels for technical assistance. This work was supported by the National Science Foundation (NSF) through the Nebraska Materials Research Science and Engineering Center (MRSEC) Grant No. DMR-1420645 (sample growth and device fabrication), NSF Grant No. DMR-1710461 (magnetotransport studies), and the Nebraska Center for Energy Sciences Research (thin film characterizations). Work by M.H. and Y.Z. was supported by the Materials Science and Engineering Divisions, Office of Basic Energy Sciences of the U.S. Department of Energy under Contract No. DESC0012704. TEM sample preparation using FIB was performed at the Center for Functional Nanomaterials, Brookhaven National Laboratory. The research was performed in part in the Nebraska Nanoscale Facility: National Nanotechnology Coordinated Infrastructure and the Nebraska Center for Materials and Nanoscience, which are supported by the National Science Foundation under Award ECCS: 1542182, and the Nebraska Research Initiative.

Conflict of Interest

The authors declare no conflict of interest.

Keywords

anomalous Hall effect, Berry phase effect, epitaxial thin film, inverse spinel, perpendicular magnetic anisotropy

Received: August 12, 2018
Revised: November 4, 2018
Published online: November 29, 2018

[1] O. Knop, K. I. G. Reid, Sutarno, Y. Nakagawa, *Can. J. Chem.* **1968**, *46*, 3463.
[2] C. F. Windisch, G. J. Exarhos, K. F. Ferris, M. H. Engelhard, D. C. Stewart, *Thin Solid Films* **2001**, *398–399*, 45.
[3] P. Silwal, C. La-o-Vorakiat, E. E. M. Chia, D. H. Kim, D. Talbayev, *AIP Adv.* **2013**, *3*, 092116.
[4] K. Dileep, B. Loukya, P. Silwal, A. Gupta, R. Datta, *J. Phys. D: Appl. Phys.* **2014**, *47*, 405001.
[5] P. Li, C. Xia, J. Li, Z. Zhu, Y. Wen, Q. Zhang, J. Zhang, Y. Peng, H. N. Alshareef, X. Zhang, *ACS Nano* **2017**, *11*, 5011.
[6] L. F. Hu, L. M. Wu, M. Y. Liao, X. S. Fang, *Adv. Mater.* **2011**, *23*, 1988.
[7] D. P. Dubal, P. Gomez-Romero, B. R. Sankapal, R. Holze, *Nano Energy* **2015**, *11*, 377.
[8] Y. G. Li, P. Hasin, Y. Y. Wu, *Adv. Mater.* **2010**, *22*, 1926.
[9] M. U. A. Prathap, R. Srivastava, *Nano Energy* **2013**, *2*, 1046.
[10] J. Marco, J. Gancedo, M. Gracia, J. Gautier, E. Rios, F. Berry, *J. Solid State Chem.* **2000**, *153*, 74.
[11] Y. Bitla, Y. Y. Chin, J. C. Lin, C. N. Van, R. Liu, Y. Zhu, H. J. Liu, Q. Zhan, H. J. Lin, C. T. Chen, Y. H. Chu, Q. He, *Sci. Rep.* **2015**, *5*, 15201.
[12] M. N. Iliev, P. Silwal, B. Loukya, R. Datta, D. H. Kim, N. D. Todorov, N. Pachauri, A. Gupta, *J. Appl. Phys.* **2013**, *114*, 033514.
[13] P. F. Ndione, Y. Z. Shi, V. Stevanovic, S. Lany, A. Zakutayev, P. A. Parilla, J. D. Perkins, J. J. Berry, D. S. Ginley, M. F. Toney, *Adv. Funct. Mater.* **2014**, *24*, 610.
[14] C. M. Zhen, X. Z. Zhang, W. G. Wei, W. Z. Guo, A. Pant, X. S. Xu, J. Shen, L. Ma, D. L. Hou, *J. Phys. D: Appl. Phys.* **2018**, *51*, 145308.
[15] P. Li, C. Xia, D. Zheng, P. Wang, C. Jin, H. Bai, *Phys. Status Solidi RRL* **2016**, *10*, 190.
[16] L. Hu, L. Wu, M. Liao, X. Hu, X. Fang, *Adv. Funct. Mater.* **2012**, *22*, 998.
[17] J. Zhang, X.-G. Zhang, X. F. Han, *Appl. Phys. Lett.* **2012**, *100*, 222401.
[18] H. Sukegawa, Y. Miura, S. Muramoto, S. Mitani, T. Niizeki, T. Ohkubo, K. Abe, M. Shirai, K. Inomata, K. Hono, *Phys. Rev. B* **2012**, *86*, 184401.
[19] P. Silwal, L. Miao, I. Stern, X. Zhou, J. Hu, D. Ho Kim, *Appl. Phys. Lett.* **2012**, *100*, 032102.
[20] P. Silwal, L. Miao, J. Hu, L. Spinu, D. Ho Kim, D. Talbayev, *J. Appl. Phys.* **2013**, *114*, 103704.
[21] S. Ikeda, K. Miura, H. Yamamoto, K. Mizunuma, H. D. Gan, M. Endo, S. Kanai, J. Hayakawa, F. Matsukura, H. Ohno, *Nat. Mater.* **2010**, *9*, 721.
[22] X. Hong, A. Posadas, C. H. Ahn, *Appl. Phys. Lett.* **2005**, *86*, 142501.
[23] R. Scherwitzl, S. Gariglio, M. Gabay, P. Zubko, M. Gibert, J. M. Triscone, *Phys. Rev. Lett.* **2011**, *106*, 246403.
[24] D. J. Groenendijk, C. Autieri, J. Girovsky, M. C. Martinez-Velarte, N. Manca, G. Mattoni, A. Monteiro, N. Gauquelin, J. Verbeeck, A. F. Otte, M. Gabay, S. Picozzi, A. D. Caviglia, *Phys. Rev. Lett.* **2017**, *119*, 256403.
[25] Z. Liao, M. Huijben, Z. Zhong, N. Gauquelin, S. Macke, R. J. Green, S. Van Aert, J. Verbeeck, G. Van Tendeloo, K. Held, G. A. Sawatzky, G. Koster, G. Rijnders, *Nat. Mater.* **2016**, *15*, 425.
[26] A. Rajapitamahuni, L. Zhang, M. A. Koten, V. R. Singh, J. D. Burton, E. Y. Tsymbal, J. E. Shield, X. Hong, *Phys. Rev. Lett.* **2016**, *116*, 187201.
[27] J. N. Eckstein, I. Bozovic, J. Odonnell, M. Onellion, M. S. Rzchowski, *Appl. Phys. Lett.* **1996**, *69*, 1312.
[28] H. Chen, Y. Gao, D. Xiao, A. H. MacDonald, Q. Niu, *arXiv:1511.02557v1*, **2015**.
[29] N. Nagaosa, J. Sinova, S. Onoda, A. H. MacDonald, N. P. Ong, *Rev. Mod. Phys.* **2010**, *82*, 1539.
[30] Z. Fang, N. Nagaosa, K. S. Takahashi, A. Asamitsu, R. Mathieu, T. Ogasawara, H. Yamada, M. Kawasaki, Y. Tokura, K. Terakura, *Science* **2003**, *302*, 92.
[31] H. Chen, Q. Niu, A. H. MacDonald, *Phys. Rev. Lett.* **2014**, *112*, 017205.
[32] S. Nakatsuji, N. Kiyohara, T. Higo, *Nature* **2015**, *527*, 212.
[33] N. Kiyohara, T. Tomita, S. Nakatsuji, *Phys. Rev. Appl.* **2016**, *5*, 064009.
[34] A. K. Nayak, J. E. Fischer, Y. Sun, B. H. Yan, J. Karel, A. C. Komarek, C. Shekhar, N. Kumar, W. Schnelle, J. Kubler, C. Felser, S. S. P. Parkin, *Sci. Adv.* **2016**, *2*, e1501870.
[35] J. Matsuno, N. Ogawa, K. Yasuda, F. Kagawa, W. Koshibae, N. Nagaosa, Y. Tokura, M. Kawasaki, *Sci. Adv.* **2016**, *2*, e1600304.
[36] K. Kuroda, T. Tomita, M. T. Suzuki, C. Bareille, A. A. Nugroho, P. Goswami, M. Ochi, M. Ikhlas, M. Nakayama, S. Akebi, R. Noguchi, R. Ishii, N. Inami, K. Ono, H. Kumigashira,

A. Varykhalov, T. Muro, T. Koretsune, R. Arita, S. Shin, T. Kondo, S. Nakatsuji, *Nat. Mater.* **2017**, *16*, 1090.
[37] H. Mizuno, K. T. Yamada, D. Kan, T. Moriyama, Y. Shimakawa, T. Ono, *Phys. Rev. B* **2017**, *96*, 214422.
[38] K. Ahadi, Z. G. Gui, Z. Porter, J. W. Lynn, Z. J. Xu, S. D. Wilson, A. Janotti, S. Stemmer, *APL Mater.* **2018**, *6*, 056105.
[39] P. J. Metaxas, J. P. Jamet, A. Mougin, M. Cormier, J. Ferre, V. Baltz, B. Rodmacq, B. Dieny, R. L. Stamps, *Phys. Rev. Lett.* **2007**, *99*, 217208.
[40] Z. B. Guo, W. B. Mi, R. O. Aboljadayel, B. Zhang, Q. Zhang, P. G. Barba, A. Manchon, X. X. Zhang, *Phys. Rev. B* **2012**, *86*, 104433.
[41] V. Keskin, B. Aktaş, J. Schmalhorst, G. Reiss, H. Zhang, J. Weischenberg, Y. Mokrousov, *Appl. Phys. Lett.* **2013**, *102*, 022416.
[42] L. Klein, J. R. Reiner, T. H. Geballe, M. R. Beasley, A. Kapitulnik, *Phys. Rev. B* **2000**, *61*, R7842.
[43] R. Mathieu, A. Asamitsu, H. Yamada, K. S. Takahashi, M. Kawasaki, Z. Fang, N. Nagaosa, Y. Tokura, *Phys. Rev. Lett.* **2004**, *93*, 016602.
[44] P. Khalifah, I. Ohkubo, B. C. Sales, H. M. Christen, D. Mandrus, J. Cerne, *Phys. Rev. B* **2007**, *76*, 054404.
[45] D. Chiba, A. Werpachowska, M. Endo, Y. Nishitani, F. Matsukura, T. Dietl, H. Ohno, *Phys. Rev. Lett.* **2010**, *104*, 106601.
[46] T. Jungwirth, Q. Niu, A. H. MacDonald, *Phys. Rev. Lett.* **2002**, *88*, 207208.
[47] S. Onoda, N. Sugimoto, N. Nagaosa, *Phys. Rev. B* **2008**, *77*, 165103.
[48] A. A. Kovalev, J. Sinova, Y. Tserkovnyak, *Phys. Rev. Lett.* **2010**, *105*, 036601.
[49] S. Onoda, N. Sugimoto, N. Nagaosa, *Phys. Rev. Lett.* **2006**, *97*, 126602.
[50] T. Fukumura, H. Toyosaki, K. Ueno, M. Nakano, T. Yamasaki, M. Kawasaki, *Jpn. J. Appl. Phys.* **2007**, *46*, L642.
[51] P. Nozières, C. Lewiner, *J. Phys.* **1973**, *34*, 901.
[52] I. A. Ado, I. A. Dmitriev, P. M. Ostrovsky, M. Titov, *Phys. Rev. B* **2017**, *96*, 235148
[53] X.-J. Liu, X. Liu, J. Sinova, *Phys. Rev. B* **2011**, *84*, 165304.